# Probing the Allende meteorite with a miniature laser-ablation mass analyser for space application

M.B. Neuland [a,*], S. Meyer [a], K. Mezger [b], A. Riedo [a], M. Tulej [a], P. Wurz [a]

[a] Physics Institute, Space Research and Planetary Sciences, University of Bern, Sidlerstrasse 5, Bern CH-3012, Switzerland
[b] Institute of Geological Sciences, University of Bern, Baltzerstrasse 1+3, Bern CH-3012, Switzerland

## ARTICLE INFO

## ABSTRACT

We measured the elemental composition on a sample of Allende meteorite with a miniature laser ablation mass spectrometer. This laser mass spectrometer (LMS) has been designed and built at the University of Bern in the Department of Space Research and Planetary Sciences with the objective of using such an instrument on a space mission. Utilising the meteorite Allende as the test sample in this study, it is demonstrated that the instrument allows the in situ determination of the elemental composition and thus mineralogy and petrology of untreated rocky samples, particularly on planetary surfaces.

In total, 138 measurements of elemental compositions have been carried out on an Allende sample. The mass spectrometric data are evaluated and correlated with an optical image. It is demonstrated that by illustrating the measured elements in the form of mineralogical maps, LMS can serve as an element imaging instrument with a very high spatial resolution of $\mu$m scale. The detailed analysis also includes a mineralogical evaluation and an investigation of the volatile element content of Allende. All findings are in good agreement with published data and underline the high sensitivity, accuracy and capability of LMS as a mass analyser for space exploration.

## 1. Introduction

The knowledge of the chemical composition of planetary bodies, moons, comets and asteroids is a key issue to understand their origin and evolution. In particular, the chemical analysis of their surfaces is of great importance on every space mission to such a celestial object, where the investigation can be conducted only remotely (McSween et al., 2011). In turn, laboratory studies of extraterrestrial material and samples returned from space were also greatly conducive to the fields of planetology and cosmochemistry (Zinner et al., 2011). In the laboratory, a variety of analytical techniques can serve to investigate in detail the samples that were returned from solar system objects (Brucato et al., 2009; Barucci et al., 2011, 2012).

For cosmochemistry, the elemental and isotopic composition of the surface material is an essential information to investigate origin, differentiation and evolution processes of the body and therefore the history of our Solar System (McSween and Huss, 2010; Wurz et al., 2009). In particular, the elemental composition, resulting in the surface modal mineralogy, gives unambiguous information about rock and soil constituents. In addition, rocks store the record of processes acting on the planetary materials (Tulej et al., in preparation). Measurements of the abundances of radiogenic isotopes provide age information on mineral and rock formation and the processes involved in their evolution. Isotope and elemental abundances provide information on planetary differentiation, geology, thermal metamorphism, volcanism, aqueous alteration and weathering processes. Such investigations may also reveal biosignatures, which makes them relevant to the search for past and present life (Wurz et al., 2009).

So far, several space missions to planets and their moons were carrying mostly orbit-based optical spectrometers for elemental analyses with limited sensitivity in element detection and spatial resolution. Spectroscopic instruments deployed on planet- or moon-orbiting spacecrafts provided data of the surface chemical composition, mostly for a few elements only and generally on a global scale (Tulej et al., in preparation). Analyses with the gamma-ray spectrometer (GRS) onboard Mars Odyssey made it possible, e.g., to compile a map of Fe, Th and K on the Martian surface (Taylor et al., 2006). Lunar Prospector's GRS and neutron spectrometer was used to infer a map of the hydrogen-abundance and the abundances of some other elements on the Lunar surface (McSween et al., 2011; Moskalenko and Porter, 2007). One pixel on the map from the Lunar Prospector's GRS data corresponds to an area of 150 km$^2$ and contains about 140 single spectra, which

* Corresponding author at: Physics Institute, University of Bern, Space Research and Planetary Sciences, Sidlerstrasse 5, CH-3012 Bern, Switzerland. Tel.:+41 31 631 4424.
E-mail address: neuland@space.unibe.ch (M.B. Neuland).

needed in total about 75 min to be recorded (Lawrence et al., 1998). Improvements of detected elements and spatial resolution have been made by employing the alpha-particle X-ray spectrometer (APXS) onboard the Pathfinder and Mars Exploration Rovers (MER) Spirit and Opportunity on the surface of Mars. These instruments enabled an extension of the former Martian surface studies by measurements of rocks and soils on the planetary surface. With a spatial resolution of a few cm and an instrument sensitivity at the per mill level, more elements could be analysed in the Martian surface. Nevertheless, environmental conditions and the long acquisition time for single measurements in the range of several hours up to days limited the efficiency of these investigations (Rieder et al., 2003).

Current and near future space missions with landers and rovers offer new possibilities for the implementation of instruments that apply in situ measurement techniques for chemical composition measurements on planetary, moon or asteroid surfaces. NASA's Mars Science Laboratory (MSL) mission, landed on Mars in early August 2012, is carrying a laser spectrometer for in situ sample analysis on Mars, applying the Laser Induced Breakdown Ionization Spectroscopy (LIBS) method, an optical spectroscopic approach. The instrument points an intense laser beam onto the sample that ablates surface material and generates a plasma plume. The emission lines of the excited atoms in the laser plasma are interpreted by spectroscopic analysis (Kim et al., 2006). Using LIBS, several elements can be measured, down to the sub per mill level. As an alternative to LIBS, lightweight mass spectrometers with high instrument performance become highly attractive for space research (Rohner et al., 2003, 2004; Managadze et al., 2010). Compared to spectroscopic methods, the mass spectrometric technique has the better analytic potential because of its much higher elemental sensitivity and the capability to detect all elements (Wurz et al., 2012). Because of the use of a focused laser beam, a high lateral and vertical resolution of chemical composition measurements is possible and this offers the opportunity of single grain investigations and therefore allows for the investigation of the heterogeneity of rocks on spatial scales of grain-size as well as studies of alteration processes on planetary surface material (Bazalgette Courrèges-Lacoste et al., 2007).

The progress in the development of miniaturised mass analysers, laser technology and fast electronics, over the last two decades, led to new opportunities for design and construction of mass spectrometers using a laser beam for ionisation of the sample material (Tulej et al., 2012). Methods like Laser Ablation Inductively Coupled Plasma Mass Spectrometry (LA ICP MS) or Laser Ionisation Mass Spectrometry (LIMS) are used frequently for measurements of trace elements at and below the ppm abundance level. Compared to LA ICP MS, LIMS offers several advantages, including simplicity of construction and operation, and the robustness of the hardware (Tulej et al., submitted for publication). The miniaturised laser mass spectrometer (LMS), developed and built in house at the University of Bern, is a LIMS instrument coupled with a time-of-flight (TOF) mass analyser. The sample material is ablated by an UV-laser pulse from a spot with a diameter of a few $\mu$m, a plasma plume is formed, and the ionised atoms are subsequently mass-analysed in a reflectron type TOF analyser. With one laser shot a complete mass spectrum can be recorded. Laser ablation TOF mass spectrometers are also part of the scientific payload of the future Russian missions Luna–Resurs and Luna–Glob to investigate the chemical composition of the lunar surface (Khartov et al., 2011).

In Bern, two prototypes LMS v1 and v2, designed for a planetary lander and rover, have been built (Rohner et al., 2003, 2004). These instruments were part of the early concept of the BepiColombo mission (Balogh et al., 2000). To build a light weight LIMS instrument, microchip lasers can be used. Their application has been tested already with these prototypes (Rohner et al., 2004).

The LAZMA instrument is the only laser ablation/ionisation mass spectrometer that was flown so far in space research. This instrument was part of the Phobos-Grunt payload (Managadze et al., 2010). Unfortunately, the mission failed due to a booster stage failure (Astronomy and Geophysics, 2012). A difference between LMS and LAZMA lies in details of ion confining and detection (Rohner et al., 2003).

Design studies revealed that an LMS flight instrument including the setup, laser system, readout card and electronics and a sample transfer system would have an average power consumption of $\sim 8$ W and would weigh $\sim 1500$ g. Assuming an ambient surface pressure of $10^{-6}$ mbar or higher on the target planet or moon, a vacuum system would be needed for operation of the LMS instrument, increasing the LMS power consumption to about $\sim 24$ W and the weight to $\sim 1650$ g (Riedo et al., 2012). For transfer of untreated rock-samples from the planetary surface to the analyser, a sample receiving unit, similar to the one designed for LAZMA (Managadze et al., 2010) would be feasible. In this design, a collecting unit places surface samples in holes on a disc, which can rotate underneath the analyser.

Recently, a combined design of the LMS instrument together with a microscopic imaging system (UV, visible and infrared) and a sample collection stage was proposed for the MarcoPolo-R mission to an asteroid (Tulej et al., submitted for publication).

For a mass spectrometer that is designed as a flight instrument for a space mission to help to answer important questions for planetary sciences, meteorites offer an excellent opportunity for evaluating its performance in the laboratory (McSween and Huss, 2010). To demonstrate the performance of LMS, element analyses on a sample of the meteorite Allende were carried out that serves as an analogue for investigations on a planetary surface in this study. Chondritic meteorites contain information about the conditions in the early solar system (Bonal et al., 2006) when they formed within the solar nebula by accretion of solid particles more than $4.5 \times 10^9$ years ago (McSween and Huss, 2010). Chondrites, in particular members of the CI group, are primitive rocks thought to originate from the outer regions of the Asteroid Belt (MacPherson and Thiemens, 2011) and represent fragments of early formed planetesimals. The Allende meteorite is a chondritic meteorite of the class CV3, possessing a complex heterogeneous structure (McSween and Huss, 2010). It consists of a mixture of accreted components, which have formed under different conditions, including a fine-grained matrix, chondrules, calcium–aluminium-rich refractory inclusions (CAIs), amoeboid olivine aggregates, metals and sulphides (Norton, 2002).

Thus investigation of this material can be challenging, but we will show that using our miniature LMS, a quantitative chemical analysis of Allende meteorite can be performed with high spatial resolution. The mass spectrometer can be used for spatially resolved chemical mapping and from these analyses the mineralogy and chemical differentiation of the material can be deduced. These performance studies offer new great possibilities for the in situ chemical analyses on planetary surfaces.

## 2. Experiments

### 2.1. Experimental setup

The LMS instrument is a miniature Laser Ablation Mass Spectrometer combined with a time-of-flight (TOF) mass analyser, developed for a planetary lander. The spectrometer has been fully designed and built at the University of Bern in the division of Space Research and Planetary Sciences. LMS has been designed to be flown on a space mission for investigation of the elemental and isotopic composition of material on the surface, e.g. regolith or
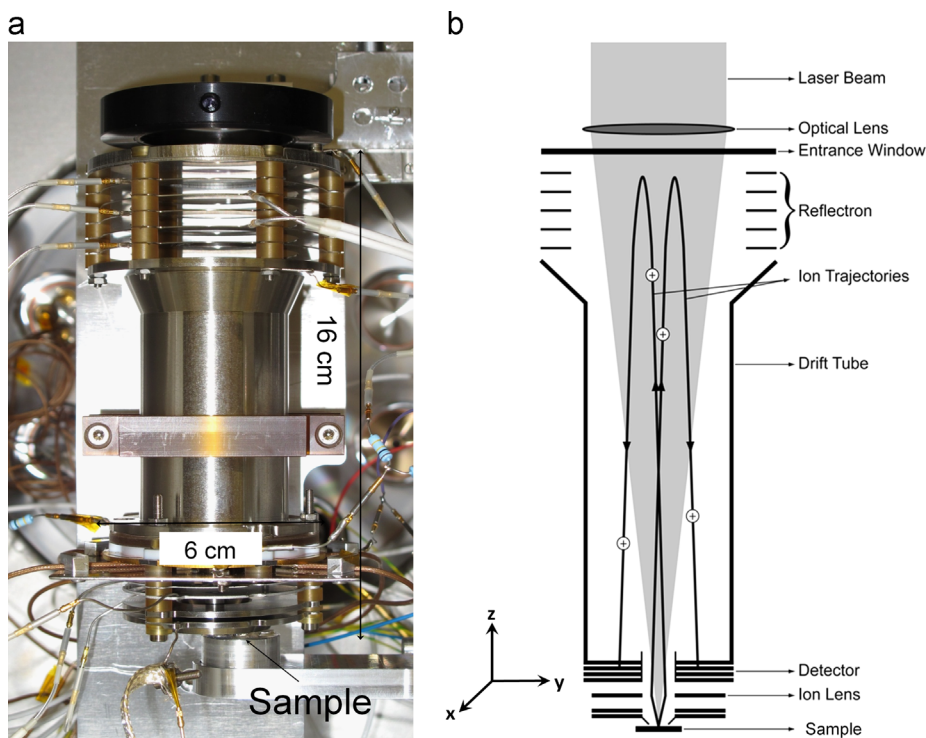
**Fig. 2.1.** The LMS setup. The LMS instrument is 16 cm high (a). For measurements, the untreated sample is placed on the aluminium holder underneath the instrument. The schematic (b) of the LMS instrument indicates the laser beam entering the instrument from the top. Two sample ion tracks are shown, illustrating typical ion trajectories from their origin at the sample surface by the ablation process to the reflectron and back to the detector. The coordinate system on the left refers to the axes of the micro-translational stage.

rocks of a planet, moon or asteroid (Rohner et al., 2003, 2004; Tulej et al., submitted for publication). A brief description of the LMS design and operation will be given hereafter. More details about design, development and construction of the LMS instrument, the detection, readout and performance as well as investigation of LMS as a flight instrument can be found in earlier reports (Rohner et al., 2003; Tulej et al., 2011, 2012; Riedo et al., 2012, 2013a).

The LMS instrument is placed in a vacuum chamber pumped down to about $10^{-8}$ mbar. A Q-switched Nd:YAG nanosecond laser system with 20 Hz repetition rate and UV output ($\lambda = 266$ nm) is used to ablate the sample. Fig. 2.1a shows the mass analyser body in the vacuum chamber and Fig. 2.1b displays a schematic diagram of the setup. The laser beam is guided into the vacuum chamber using dielectric mirrors and is focused on the sample by an optical lens. The laser beam passes all the way down along the ion optical axis of the instrument until it hits the sample. Laser interaction with the sample surface causes ablation and atomisation of the surface material. In the plasma plume that is formed, the atoms are ionised. The released ions enter the mass analyser and become confined via ion optics. The separation of the ions occurs on the way through a field free drift tube to the multichannel plate (MCP) detector, which they reach after being mirrored by the reflectron (Fig. 2.1b). Ions having the same $m/q$ are detected as a signal pulse after a time-of-flight (TOF) that is proportional to $m/q$, where $m$ is the mass of the ion and $q$ its charge.

The LMS analysis does not require any sample treatment or conditioning, therefore elemental and isotopic abundances in any kind of solid sample can be analysed directly. This reduces the risk of sample contamination in the laboratory and prevents sample loss. To move the sample inside the UHV chamber, it is placed on a micro-translational stage, which allows pointing the laser spot on defined locations on the sample surface in the $x$–$y$-plane (Fig. 2.1) with 2 μm position accuracy.

The detector consists of two micro channel plates (MCP) in Chevron configuration. The MCP signal is collected by four concentric anode rings and read out by a PCI standard high-speed ADC card. The laser pulse, releasing the ion plume, gives the initial trigger for the data acquisition. TOF-spectra are recorded for the duration of 20 μs, which is converted to a mass range of 1 to 250 amu/q (see Section 2.3). Every single laser shot results in a complete mass spectrum. With an averager mode of the read out card firmware the spectra of 100 laser shots are combined to reduce noise. The acquisition card software also provides a direct display of the measured and averaged signal over TOF scale, which allows monitoring the measurement in real time.

The ADC card, used in this study, allows recording of TOF spectra with a dynamic range up to 7 orders of magnitude (Riedo et al., 2012). Three acquisition channels of the ADC card are used with different signal amplification factors to record the TOF spectra with sensitivity to major and minor elements. In the high gain (HG) channel, minor and trace elements are visible, but major element peaks are saturated. Major elements are recorded correctly by the low gain (LG) channel. Additionally, a medium gain (MG) channel is used, having an overlapping sensitivity range with HG and LG, to ensure linearity over the entire dynamic range. By combining all three channels, a dynamic range of up to 9 decades can be obtained (Riedo et al., 2012). Fig. 2.2 shows an example of a mass spectrum of the Allende sample. All three channels are displayed, each with a dynamic range of 4–5 decades.

Before launching a measurement campaign, the set of LMS voltages of lenses, reflectron, MCPs as well as the laser irradiance were optimised to reach the desired mass resolution and the best detection sensitivity for elements of interest. These settings for ablation, ionisation and detection depend not only on the sample texture, like porosity and rigidity, but also on the sample composition, e.g. the volatility. To find the suitable instrument settings in the laboratory, an optimiser software based on an adaptive particle swarm algorithm is used. After a few calibration measurements the best settings regarding mass resolution, signal intensity and sensitivity are usually found. For more details about the optimiser system
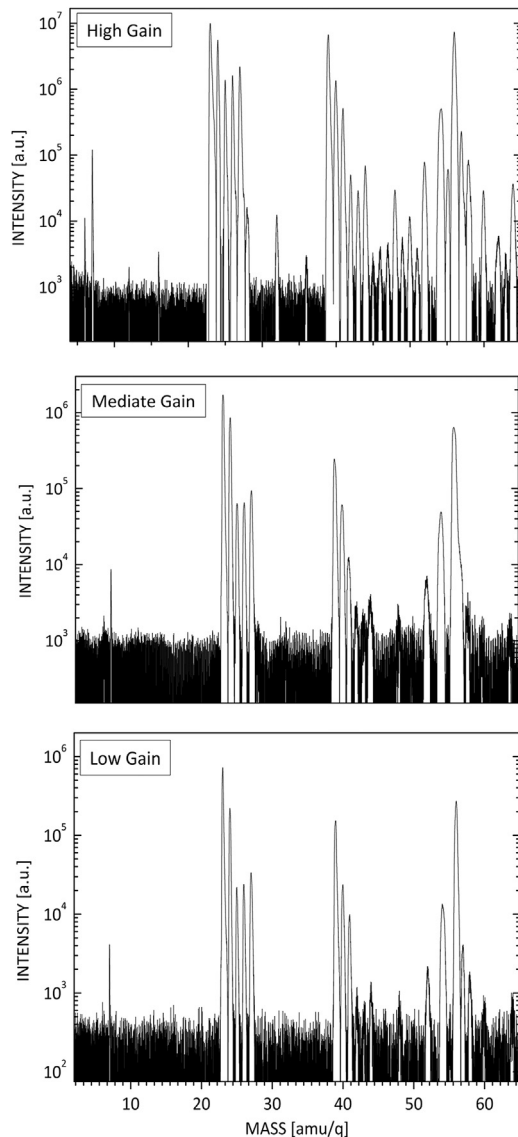
**Fig. 2.2.** Dynamic range. This figure displays a typical data set for one measurement on the Allende sample showing the high gain (HG), medium gain (MG) and low gain (LG) channels, which are recorded simultaneously. Each spectrum is the sum of 50,000 individual spectra. By combination of all three channels, a dynamic range of 9 decades can be obtained.

it is referred to recent publications (Bieler et al., 2011; Riedo et al., 2012). This instrument optimisation is necessary to achieve repeatable and quantitative results. The optimisation procedure will be performed on an instrument in space in an autonomous manner.

## 2.2. Allende sample and measurement procedure

For simplicity of the analyses and better visualisation of the investigated regions, a flat surface of Allende sample was used. It was cut from a larger piece of the meteorite with a dry diamond blade. The sample is of trapezoidal shape with a base of 13 mm, a height of 10 mm and a thickness of 2.73 mm, as shown in Fig. 2.3a. This picture allows distinguishing the variety of chondrules and inclusions in the meteorite.

After the mass spectrometric studies, a thin section of the sample was made, which is shown in Fig. 2.3c in transmitted light. Though the thin section exposes a layer approximately 100 μm underneath the analysed surface, the optical investigation of the thin section can help to place the mass spectrometric measurements

and the resulting chemical compositions into a mineralogical context (Section 3.2).

The locations where the measurements were performed are marked by symbols in Fig. 2.3b. The measurement area has a dimension of approximately 6 mm × 3.6 mm. The measurement campaign on the Allende meteorite consisted of 138 measurements with a horizontal spacing of 600 μm and a diagonal spacing of 426 μm (Fig. 2.3b). The micrometer stage allows steps of few μm, but the aim of this campaign was to cover a larger area of the sample surface area with a satisfactory density of measurements to draw conclusions on the elemental compositions in very precisely located small single spots. Fig. 2.3b shows the distribution of the measured spots on the sample surface. The *x*- and *y*-axis labels describe the position and correspond to the micrometer-stage coordinate system (refer to Fig. 2.1).

Though the sample was cut to a flat surface prior to the measurements, relatively large cavities and holes are still present in the sample surface. Additionally, porosity of the sample material and inhomogeneous distribution of material occasionally causes effects that lead to cratering induced by the focused laser beam that exceed the expected laser spot diameter. The micro-translational stage was moved only horizontally (in *x*- and *y*-direction in Fig. 2.1) during the measurement campaign. The distance between sample and entrance electrode (*z*-direction in Fig. 2.1) was not changed and kept at 1 mm, because the surface was flat. In addition the used laser irradiances were defined before and held constant during the measurement campaigns. As a consequence the ions could not be focused, where large cavities and holes prevailed. The spectra for these few particular cases are not considered further.

For an LMS instrument operating in space on a planetary surface, collected samples would also exhibit cavities and holes and cutting the samples to a flat surface would not be possible. For a LMS flight instrument, an aperture in front of the electrode, acting as a distance holder could be implemented. Such a device would provide the accurate distance to the sample so that the laser focus lies on the sample surface (Rohner et al., 2003). Using a sample disc on a planetary rover, the accurate distance of sample surface to the entrance electrode would directly be given by the geometry of the sample disc and the depth of the holes (Managadze et al., 2010).

For each investigated location in this study of Allende, the measurement file contains the data of 500 waveforms, where one waveform represents a TOF spectrum, which is the result of the accumulation of 100 single-shot spectra (Section 2.1). Thus, every single measurement contains the signal from 50,000 single laser shots. It takes approximately 40 min to record these spectra with the current setup and thus ∼100 h to conduct all 138 measurements. The data are stored for all three channels simultaneously in one file with the used gain parameter, laser irradiance and position on the sample.

In the optimisation procedure (Section 2.1), laser irradiances in the range 0.5 to 0.8 GW/cm$^2$ were found to yield to the best mass resolution, highest signal intensity and sensitivity to the elements of interest in the Allende sample. More precisely, four slightly different laser irradiances 0.5, 0.6, 0.7 and 0.8 GW/cm$^2$ were applied in the measurement campaigns to investigate also a possible dependence of laser ablation conditions on the detection sensitivity to different elements (Section 2.4). The shot-to-shot uncertainty in the laser irradiance is typically less than 40% (Riedo et al., 2013a) and is mainly caused by the strong dependence of laser irradiance variations on the accuracy of the focus point.

Some of the sample regions were analysed with higher spatial resolution, when for example a chondrule or an inclusion was spotted by the laser beam. With the direct monitoring software such regions were identified immediately during the measurements because of remarkable changes in the observed TOF spectra, e.g. higher abundance of single elements. In such a case additional
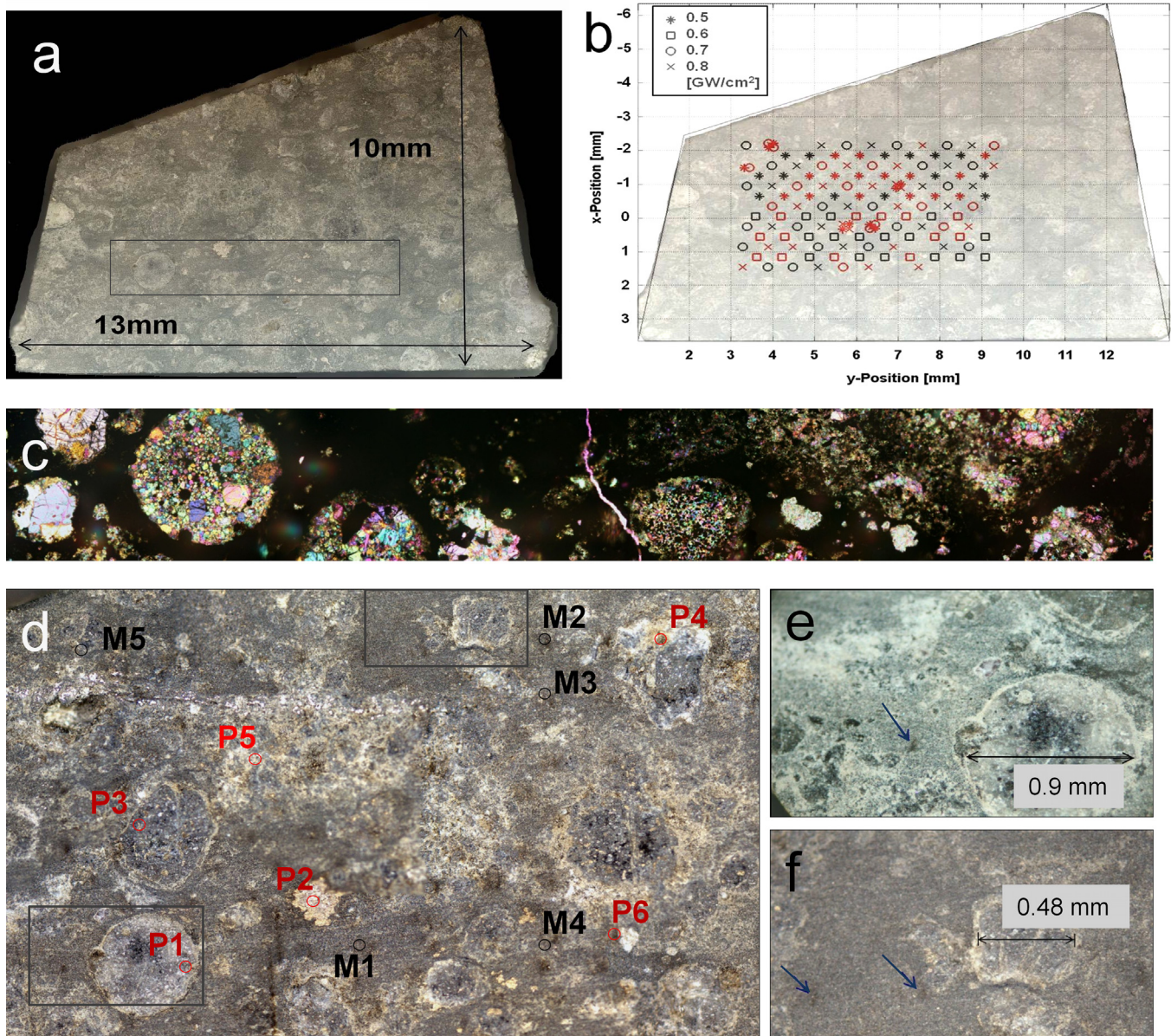
**Fig. 2.3.** Allende sample, measurements and laser shots. (a) Allende sample. (b) Locations of the 138 measurements on the sample in a rectangular area of 6 mm × 3.6 mm. Ablation pits by different laser irradiances are indicated by colour symbols (see legend). Black symbols refer to matrix-measurements, red labels to other locations. (c) Detailed view of the Allende thin section (box shown in the panel a)). (d) The image shows in detail the rectangular region of the measurement area after the measurement campaign. Positions of laser ablation pits can be located. The marked rectangular regions are shown in detail in panel (e) and (f). The indicated labelled points (P1 to P6 and M1 to M5) refer to analyses in Section 3.4. (e) and (f) Zoom of the rectangles indicated in panel (d). The chondrules are ca. 0.9 mm and 0.48 mm across. Blue arrows point to craters generated by the focused laser beam (50,000 shots). The diameter of the craters is approximately 20 μm.

measurements with a diagonal spacing of 85 μm were carried out around these spots (see Fig. 2.3b). These positions, where such remarkable data were observed during the measurement procedure, could be directly related to chondrules, inclusions or (Fig. 2.3a and b). It is foreseen to implement a camera system into LMS to be able to select locations of special interest on a surface of a sample (Section 4) already when planning the measurements (Tulej et al., submitted for publication).

### 2.3. Data processing

The raw data of the LMS measurements are stored in the form of time-of-flight spectra with the signal from the three different channels HG, MG and LG (see Fig. 2.2). Conversion from TOF- to

mass-scale is done by conducting a calibration according to

$$m/q = k_0 \times (t - t_0)^2 \qquad (1)$$

where $m/q$ is the mass/charge ratio, $t$ the time of flight and $t_0$ and $k_0$ are calibration constants. By performing a linear regression, the constants can be determined accurately with a typical accuracy of $10^{-3}$ (Riedo et al., 2012). The parameters $t_0$ and $k_0$ were determined for every TOF spectrum individually. The spectra in HG, MG and LG have also been calibrated separately. As a result, similar calibration constants were determined for all measurements of the campaign. The averaged calibration constants for HG and LG are listed in Table 2.1 as an example for all four applied laser fluences. The uncertainties are expressed thru the statistical error due to linear regression and the error resulting from averaging $\sim 30$ measurements for each of the laser irradiances. For the individual

**Table 2.1**
Calibration constants.

| Laser Fluence | 0.5 GW/cm$^2$ | 0.6 GW/cm$^2$ | 0.7 GW/cm$^2$ | 0.8 GW/cm$^2$ |
|---|---|---|---|---|
| $k_0$ (HG) [amu/C(ns$^2$)] | $1.722 \pm 0.002$ | $1.726 \pm 0.001$ | $1.724 \pm 0.002$ | $1.724 \pm 0.002$ |
| $k_0$ (LG) amu/C(ns$^2$)] | $1.711 \pm 0.002$ | $1.714 \pm 0.001$ | $1.714 \pm 0.002$ | $1.714 \pm 0.002$ |
| $t_0$ (HG) [ns] | $-52.49 \pm 1.42$ | $-51.55 \pm 1.27$ | $-52.30 \pm 2.48$ | $-52.05 \pm 2.33$ |
| $t_0$ (LG) [ns] | $-52.53 \pm 2.10$ | $-52.41 \pm 1.83$ | $-52.01 \pm 2.61$ | $-51.41 \pm 3.07$ |

laser irradiances the relative errors are only about 0.12% or lower for $k_0$ and approximately 5% or lower for $t_0$. The observed difference of calibration factors in HG, MG and LG is due to the slightly different ion arrival times to different anode rings of the detector (Section 2.1). This results from a small difference in geometry of the ion tracks and leads to minor variation in the calibration coefficients.

After calibration, the LMS data were evaluated automatically. Previous software investigation had shown that mass peaks can still be assigned to their real masses, if the calibration constant $k_0$ does not deviate more than 0.2% from its correct value for masses 1 … 125 amu and not more than 0.1% for masses up to 250 amu. For $t_0$ it was found that a deviation of 12% from the correct value does not cause a problem for masses smaller than 175 amu. For higher masses $t_0$ should not deviate more than 8%. These numbers show that for the elemental analyses the mass calibration of every single measurement is accurate enough for automatic evaluation of the elemental abundances by the analysis software.

The mass error $\Delta m/m$, i.e., the deviation of a calibrated mass of a certain isotope to its literature mass value, is on average about $\sim 10^{-5}$ for the Allende campaign. The mass resolution is about 300 for these measurements, which is high enough to conduct accurate elemental analysis of mineralogical samples.

The following analysis steps are performed automatically by a MATLAB based software. This software package, developed for the analysis of LMS elemental composition data, evaluates all the mass lines in the spectra. For each measurement, peak detection, fitting and area determination are carried out, the data from HG, MG and LG are correlated and processed, isotopes are assigned to the peaks and the elemental composition of the measurement is computed.

The determination of elemental abundances is performed by integration of the individual mass peaks in the HG, MG and LG spectra. For the determination of the peak areas, a Gaussian fit is applied to the individual peaks, separately for the mass spectra in the different channels. A Gauss function describes the mass peaks of LMS measurements sufficiently precise for elemental analysis, which has been investigated and shown in previous studies (Tulej et al., 2012). The peak boundaries for the integration of an individual peak are determined by a zero crossing algorithm and the local background is modelled by a linear function. A mass peak is only considered for further analysis if the fit with a Gaussian function of least square type reaches a precision of $10^{-8}$. The residuals between Gauss-function and data points result in an error of the computation of the peak-area. This error is taken into account for the full error propagation in the following analysis.

In the course of data processing, HG, MG and LG spectra are scaled by the corresponding gain factors to make use of the complete dynamic range from all three channels. After scaling, for one specific mass peak, the mean value of the peak areas from all three channels is processed. If a peak is saturated in HG, and therefore its assigned element concentration is much lower than in MG and LG, the mean is taken only from the latter two channels. Fig. 2.4 shows an example of a typical measurement of the Allende campaign for a mass spectrum with calibrated mass scale in the HG channel. The very intense peaks, e.g. the peaks of Mg and Al, are saturated in the HG channel. Therefore these peak areas are
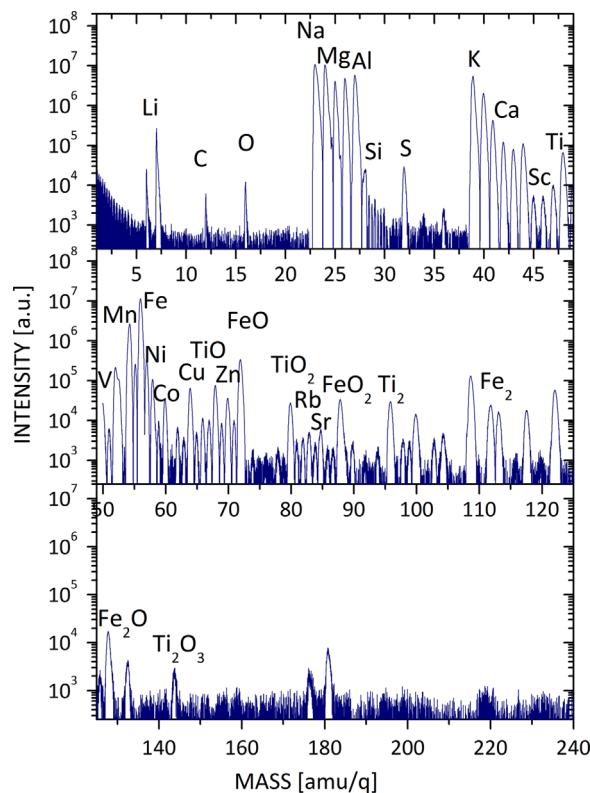


**Fig. 2.4.** Mass spectrum of Allende (HG). Typical LMS measurement on the Allende sample (HG) with some elements assigned. The intensity is displayed in arbitrary units.

evaluated using only MG and LG spectra. The saturation can also be recognized by the slight deformation of the peak tip. In HG unsaturated peaks, like S or Ti e.g., have a symmetric Gaussian-like shape. Only by use of the HG data, isotopes like $^{34}$S, minor elements like C and Sc are detected as well as Mn and Co.

For determination of elemental composition, the mass peaks of the isotopic component are considered with their natural abundances, which are taken from Becker (2007). Formally, for an element having three isotopes we calculate

$$A_{El} = \frac{A_{Iso1}}{Ab_1} = \frac{A_{Iso2}}{Ab_2} = \frac{A_{Iso3}}{Ab_3} \qquad (2)$$

where $A_{Iso1}$, $A_{Iso2}$ and $A_{Iso3}$ stand for the areas of the respective isotopes calculated from the mean of all three channels, $Ab_1$, $Ab_2$ and $Ab_3$ for the terrestrial abundance of each isotope (from (Becker, 2007)) and $A_{El}$ for the resulting scaled area of the element.

In the analysis algorithm, several criteria like the number of detected isotopes, their isotopic abundance and the signal-to-noise-ratio (SNR) are evaluated, before the value of $A_{El}$ is derived from the mean of different isotope areas. E.g. the Ca abundance in the sample is obtained from the isotopes $^{42}$Ca and $^{44}$Ca rather than from $^{40}$Ca, as this peak is surrounded by the highly saturated peaks

of $^{39}$K and $^{41}$K, that are due to terrestrial contamination of the Allende sample (Section 3.2).

Similar complications in the analysis can arise from isobaric interferences that are caused by oxides and clusters that may be released from the surface or formed by plasma chemistry (Tulej et al., 2012). Oxides and clusters can readily interfere with isotopes heavier than 62 amu ($Z \geq 28$, see Fig. 2.4) albeit their abundances are clearly reduced in comparison to our previous studies (Tulej et al., 2012). However, other studies have shown that for laser ablation with irradiances of $\leq 1$ GW/cm$^2$, the oxide signals are only a small fraction of the element signal (Figg et al., 1998; Russo et al., 2002), which is also the case in the present study. Furthermore, checking isotopic abundances during the data processing assures that peaks with isobaric interferences are identified and not used for elemental abundance calculations. For the present study, analyses of the Allende data were performed for masses lighter than 62 amu, i.e., for the elements C, Mg, Al, Si, S, Ca, Sc, Ti, V, Cr, Mn, Fe, Co and Ni.

## 2.4. Relative sensitivity coefficients

For the quantitative analyses of the elemental compositions of solid materials, the instrument has to be calibrated by measuring the elemental composition of standard research materials (SRM). Direct, quantitative analyses by laser ionisation mass spectrometry are to date not possible albeit investigation with a few LIMS systems are promising (Brinckerhoff et al., 2000; Huang et al., 2011; Riedo et al., 2013b).

Due to very different chemical properties of the different elements (e.g. ionisation potentials, sublimation temperature), the ionisation efficiencies for various elements during ablation with a nanosecond laser are a complex function of ablation conditions (e.g. pulse duration, wavelength, laser focus diameter) (Tulej et al., 2012). Moreover, compositional effects and sample morphology (matrix effects) can further complicate the quantitative analysis. Therefore the so-called relative sensitivity coefficients (RSCs) have to be obtained at least for all elements of interest as follows Becker (2007).

$$RSC = \frac{\text{experimentally measured element concentration}}{\text{literature element concentration}} \quad (3)$$

Using standard reference materials (SRM) of known certified composition offers a possibility for RSC determination, but these artificial samples have very different texture and composition from natural rocky material. Hence for laboratory studies on extraterrestrial samples like the one on hand, it is the best suitable method to carry out a bulk measurement and to compare with literature data that results from other measurement techniques and therefore serves as an independent reference.

In an earlier LMS configuration, where an IR laser was used, the dependence of RSCs on the elements' ionisation potentials and boiling temperatures was observed (Tulej et al.2011). Owing to the shorter wavelength of the UV laser used in this study, only a moderate dependence of RSCs on ionisation potentials is expected (Amoruso et al., 1999).

Fig. 2.3d shows the part of the sample surface where 138 measurements with high spatial resolution were conducted. Seventeen of these measurements are accumulated around locations of special interest and are not part of the regular pattern (Fig. 2.3b). By relocating the laser shots on the sample surface (Fig. 2.3b and d), the ones probing meteorite matrix, could be distinguished. These resulted in 66 measurements optically located on matrix material, shown in Fig. 2.3b in black. In contrast, the 55 regular and the 17 additional measurements that were found to be located on an inclusion, a chondrule or the like, are displayed in Fig. 2.3b in red. This means that 54.4% of the measurements, accomplished in regular intervals, are on matrix material. In comparison, 60 vol%

of Allende are known to consist of matrix material (Norton, 2002; Clarke et al., 1971).

Hence the 66 measurements on the matrix were used to determine the RSCs by dividing the abundance value determined from the measured LMS spectra by literature elemental abundances of CV carbonaceous chondrites (CC) from Lodders and Fegley (1998). An exclusion criterium in the analysis software assured that for the RSC of a single element, peak areas that obviously differed from the average were not taken into account. This was the case for highly abundant elements, i.e. Mg and Fe, in three measurements, where the main isotope peak ($^{24}$Mg, $^{56}$Fe) caused saturation in the HG and sometimes even in the MG channel and degradation of the isotope peaks following at higher masses. Additionally, in two other spectra from the matrix measurements, the element peaks of Ni and Co showed a value of more than 3σ away from the average of all 66 measurements and were therefore disregarded. This procedure is eligible as the entity of all 66 measurements on the matrix shows a clear uniformity (Fig. 3.3a) for all analysed elements.

The literature values are reproduced in Table 2.2. These numbers are derived from electron microprobe analyses, neutron activation and wet chemical analyses (Lodders and Fegley, 1998). To use a data set for specifically Allende matrix or Allende bulk as a reference instead of CV CC would not essentially change the RSCs in their shown precision. Data sets for Allende bulk and matrix can be found in Table 3.1 and Table 3.2 in the last column each. These are later used for comparison with the LMS results.

Not all elements could be determined in every LMS measurement on the Allende sample. This can be due to a very small RSC value and therefore being at the lower limit of detection or due to very low concentration of the element. Therefore the RSCs for the elements C, Mg, Al, Si, S, Ca, Sc, Ti, V, Cr, Mn, Fe, Co and Ni were calculated using

$$RSC_X = \frac{1/n_x \times (\Sigma_i A_i^X / \Sigma_i A_i^{\text{tot}})}{(P_X / \Sigma_i P_i^{\text{tot}})} \quad (4)$$

where $X$ stands for a particular element and $i$ for the measurement number. $A$ designates the area of the peak in the mass spectrum scaled and converted to the corresponding amount of the element; therefore $A_i^X$ defines the area of element $X$ in measurement $i$. Accordingly, $A_i^{\text{tot}}$ gives the sum of the areas of all elements in measurement $i$. The ratio of these two sums $\Sigma A_i^X$ and $\Sigma A_i^{\text{tot}}$ corresponds to the experimentally measured concentration of element $X$. In the same manner, the certified element concentration is the ratio of an expected concentration $P_X$ for element $X$ (Table 2.2) and the fraction $P_i^{\text{tot}}$ that corresponds to all elements in this one spectrum. The resulting value has to be divided by $n_X$, the number of measurements, where element $X$ was contained.

A set of RSC values has been evaluated for every laser irradiance applied in this study (0.5, 0.6, 0.7 and 0.8 GW/cm$^2$). If, for one laser irradiance, an element was detected in less than 25% of the

**Table 2.2**
Elemental abundance in CV carbonaceous chondrites.

| Element | Atom-%[a] | Element | Atom-%[a] |
|---------|-----------|---------|-----------|
| C | 1.0640 | Ti | 0.0438 |
| Mg | 14.1871 | V | 0.0046 |
| Al | 1.5014 | Cr | 0.1614 |
| Si | 13.4794 | Mn | 0.0667 |
| S | 1.6544 | Fe | 9.8867 |
| Ca | 1.1070 | Co | 0.0262 |
| Sc | 0.0006 | Ni | 0.5423 |

[a] Concentrations are taken from Lodders and Fegley (1998) and converted from weight-% into atom-% using the corresponding atomic weights from Becker (2007).

**Table 2.3**
Relative sensitivity coefficients (RSCs).

| Element[a] | Energy of first ionisation $I_e$ [eV][b] | Relative sensitivity coefficients (RSCs) at laser irradiance | | | |
|---|---|---|---|---|---|
| | | 0.5 GW/cm² | 0.6 GW/cm² | 0.7 GW/cm² | 0.8 GW/cm² |
| C | 11.260 | – | – | $0.0021 \pm 0.0003$ | $0.0017 \pm 0.0003$ |
| Mg | 7.646 | $0.309 \pm 0.004$ | $0.270 \pm 0.004$ | $0.822 \pm 0.004$ | $0.991 \pm 0.005$ |
| Al | 5.986 | $1.750 \pm 0.015$ | $2.278 \pm 0.012$ | $1.264 \pm 0.005$ | $1.525 \pm 0.006$ |
| Si | 8.151 | – | – | $0.0003 \pm 0.0001$ | $0.0003 \pm 0.0001$ |
| S | 10.360 | – | – | $0.0068 \pm 0.0003$ | $0.0024 \pm 0.0002$ |
| Ca | 6.113 | $3.89 \pm 0.2$ | $4.11 \pm 0.05$ | $1.59 \pm 0.04$ | $1.22 \pm 0.04$ |
| Sc | 6.54 | – | – | $3.125 \pm 0.244$ | $1.847 \pm 0.256$ |
| Ti | 6.82 | $1.97 \pm 0.09$ | $2.06 \pm 0.16$ | $0.77 \pm 0.01$ | $0.51 \pm 0.02$ |
| V | 6.74 | $3.94 \pm 0.14$ | – | $0.85 \pm 0.08$ | $0.50 \pm 0.06$ |
| Cr | 6.766 | $2.75 \pm 0.05$ | $1.82 \pm 0.05$ | $1.50 \pm 0.01$ | $1.54 \pm 0.01$ |
| Mn | 7.435 | – | $0.42 \pm 0.07$ | $0.60 \pm 0.02$ | $0.42 \pm 0.01$ |
| Fe | 7.870 | $2.16 \pm 0.02$ | $1.57 \pm 0.01$ | $1.741 \pm 0.008$ | $1.722 \pm 0.009$ |
| Co | 7.86 | – | – | $0.487 \pm 0.004$ | $0.087 \pm 0.002$ |
| Ni | 7.653 | – | $0.19 \pm 0.05$ | $0.188 \pm 0.004$ | $0.131 \pm 0.003$ |

[a] Elements are sorted ascending by their atomic number.
[b] Energy of first ionisation was taken from Becker (2007).

measurements, no RSC was evaluated. The complete list of RSC values calculated and used for analysis is displayed in Table 2.3. It can be seen that for the lower laser irradiances fewer RSCs could be determined, because LMS is more sensitive to certain elements, e.g. C, S, Sc or Co, when higher laser power is used. The uncertainty, given with every RSC value includes the error introduced by the peak fitting process itself (Section 2.3).

Fig. 2.5 depicts the correlation between the literature data for chondrites of class CV (from (Lodders and Fegley, 1998)) and the abundances on Allende measured by LMS. The experimental RSC therefore corresponds to the perpendicular distance of one data point to the diagonal in this figure. The diagonal solid line shows the optimal case of RSC=1. This correlation plot illustrates that elements like Si or S have small RSC values and therefore deviate more from the diagonal line.

A rough correlation between the RSC values and the first ionisation energy of the elements is observed, as also reported in previous LMS studies (Tulej et al., 2011) and by other groups (Zhang et al., 2013). Elements with similar ionisation energies lie on or close to lines parallel to the diagonal (dashed lines in Fig. 2.5), which would be a RSC=1, meaning that they have approximately the same RSCs. The ionisation energies are listed in Table 2.3 in the second column. For example, Ni, Mn and Mg all have ionisation energies of ~7.5 eV and are close to one, i.e. the diagonal line in Fig. 2.5. C and S, on the other hand, both having ionisation energies of ~11 eV, have almost the same RSCs and lie on a separate line with lower RSC. Of course, RSCs are not only dependent on ionisation energy. The residual variations of RSCs for elements with comparable ionisation potentials arise from other physical properties of the elements and far-reaching processes in the laser ablation and ionisation processes (Bulgakova et al., 2000; Harilal et al., 2003; Xie et al., 2011).

Especially at two of the higher laser power densities, 0.7 and 0.8 GW/cm², RSCs are observed to be about unity, which means directly quantitative representation of the elements in the mass spectra while measuring. However, the RSC-scaling procedure of individual elements does not represent an obstacle for analysis owing to highly accurate and precise RSC values (Table 2.3).

The relative sensitivity coefficient (RSC) describes how sensitive the LMS instrument (y-axis) is to detection of a certain element. Comparing to a reference value for chondrites of class CV from Lodders and Fegley (1998), the RSCs can be illustrated.

In an earlier campaign on a sample of Allende, where measurements on 30 positions using laser irradiances of ~0.3–0.4 GW/cm²
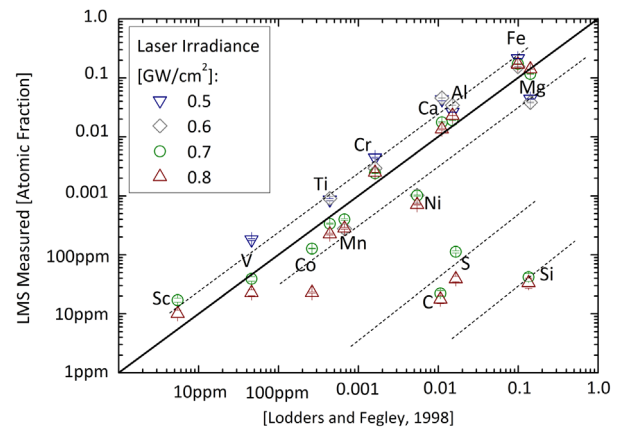


**Fig. 2.5.** RSC correlation plot. The relative sensitivity coefficient (RSC) describes how sensitive the LMS instrument (y-axis) is to detection of a certain element. Comparing to a reference value for chondrites of class CV from Lodders and Fegley (1998) (x-axis), the RSCs can be illustrated.

were applied, we determined similar RSC values as listed in Table 2.3. Additionally, we derived RSCs from measurements we did on a pellet of Allende (powderised and pressed bulk material of Allende) using a very low laser irradiance of 0.4 GW/cm². For the elements, where calculation of RSCs was possible for such low laser irradiances, comparable values of RSCs were determined (Fig. A.1).

In independent studies, NIST standard reference materials (SRM) have been investigated using the same LMS setup. Following the similar analysis procedure like in this study of Allende, spectra were recorded and RSCs were calculated (Meyer, 2013). Taking into account that the used standard samples differ extremely from planetary surface material in terms of morphology, structure and chemical composition, still the resulting RSCs are in comparable range (Fig. A.1). The NIST sample SRM665 e.g. consists of about 99% Fe. Therefore the mass peak of Fe will always be saturated and thus also the resulting RSC is not a reliable reference. For measurements with a laser irradiance of 0.914 GW/cm², an RSC for Al of $1.220 \pm 0.471$ and $0.722 \pm 0.171$ for Mn was determined for SRM665 (Meyer, 2013). Comparing these values on extremely different samples from the studies of (Meyer 2013) to the figures in Table 2.3 assures the reliability of the used RSC sets for the Allende study. Appendix A can be consulted for more explanation on RSCs of other samples and the correlation to ionisation energy.

# 3. Results and discussion

## 3.1. Estimation of LMS sample consumption

Fig. 2.3a shows the surface of the investigated meteorite and Fig. 2.3d the rectangular shaped region of the sample, which was investigated in this study. The regions marked in Fig. 2.3d are shown in Fig.2.3e and f in an enlarged scale for more detailed analysis of the laser spots. Each of these cut-outs contains a chondrule and one or two measurement spots on a matrix-like light grey surface with laser irradiances of 0.7 GW/cm$^2$ (Fig. 2.3e) and 0.7 and 0.8 GW/cm$^2$ (Fig. 2.3f). The dimensions of the chondrules are approximatey 0.9 mm and 0.48 mm across. Comparing the measurement spots, marked by the arrows in Fig. 2.3e and f, the diameter of these can be estimated to be ∼25 μm each. As the exact crater drilled by the laser is too small to be optically resolved and the size measurement is done from the visible dark region on the surface sample, the real crater is thought to be smaller with a diameter of ∼20 μm, which is in accordance to earlier studies (Rohner et al., 2003; Wurz et al., 2009; Riedo et al., 2012). The dark spot on the sample surface is assumed to be larger due to the formation of a crater rim of ablated material, which formed from melted and evaporated material during the laser irradiation.

The Allende meteorite sample is of trapezoidal shape with a base width of 13 mm and a height of approximately 10 mm (Fig. 2.3a). As the thickness of the sample is 2.73 mm its volume is 0.27 cm$^3$. A single measurement creates a crater with a diameter of approximately 20 μm. Based on current LMS experiments with different laser irradiances on metallic samples and other publications on the topic investigating laser ablation with much higher irradiances (Yu et al., 2009; Lin et al., 2010), we estimate that the craters created by 50,000 laser shots on the meteorite surface are about 0.1 μm deep. Using this estimate, 50,000 laser shots in one measurement will remove a volume of approximately 1•10$^{-11}$ cm$^3$. With the average density of Allende of ∼3 g/cm$^3$ (Consolmagno and Britt, 1998; Clarke et al., 1971), this corresponds to a consumption of approximately 30 pg of sample material for one measurement location and a sample consumption of only fg per laser shot. Assuming further an average mass of about 20 amu of the

analysed atoms and an ionisation efficiency of 0.01 in the ablation and ionisation process this yields to approximately 2•10$^5$ ions per laser shot.

Consequently, a series of 100 measurements, like the Allende campaign for this study, results in a total sample consumption of ∼3 ng for a representative bulk analysis (Section 3.2). Thus LMS can be well considered as an instrument performing essentially non-destructive measurements with minimal sample consumption.

## 3.2. Elemental composition and mineralogy of Allende

The mass spectrometric measurements on the Allende sample reveal a very high content of Li ($^6$Li and $^7$Li), Na ($^{23}$Na) and K ($^{39}$K and $^{41}$K) (see example mass spectrum in Fig. 2.4). The high concentration of these elements is of terrestrial origin and caused by contamination of the sample prior to LMS analyses. Such terrestrial contaminations can compromise the analyses but they are not relevant for an LMS instrument operating in space. For the Allende campaign, the concentrations of C, Mg, Al, Si, S, Ca, Sc, Ti, V, Cr, Mn, Fe, Co and Ni were determined in situ on the locations where measurements were taken (Fig. 2.3b). The element concentrations measured with LMS on Allende are reported in Tables 3.1 and 3.2. The values are determined by the analysis of the area of each element peak (Eq. (2)) relative to the total elemental content of the measurement, resulting in atomic fractions. Tables 3.1 and 3.2 are the result of applying the RSCs from Table 2.3 to each element contained in the measurements. The elements are sorted according to their cosmochemical properties (McSween and Huss, 2010), i.e., according to their 50% condensation temperatures. The results are presented as atomic fraction of an element, i.e. the fraction of atoms in a portion of Allende being of the noted atom species.

The values in Table 3.1 are the mean values of all measurements on the Allende matrix (black symbols in Fig. 2.3b). For comparison, the table displays also element concentrations for the Allende matrix samples from (Clarke et al., 1971). The analysis in Clarke et al. (1971) is based on electron microprobe investigations of a dust sample of Allende matrix weighing approximately 2 g. For comparability reasons, the elemental concentration data was converted to atomic fractions. It should be emphasized that LMS allows an evaluation of major and trace elements during one measurement. In contrast to other methods, LMS allows to determine the elemental content of V and Sc, which are present only at the ppm level in Allende.

A good agreement between the published values (Clarke et al., 1971) and our measurements is found, within the uncertainties for major elements. For refractory elements, i.e., Co, Al, and Cr, we find in the LMS measurements higher abundances than reported in Clarke et al. (1971). This can be explained by the high spatial resolution and the small sample consumption of LMS. LMS analyses only a few nanograms of material in a laser spot with a diameter of ∼20 μm (Section 3.1) and thus small and localised refractory inclusions can have a large effect in the abundance measurements. If in the LMS measurements, few single grains consisting of e.g. the minerals chromite [(FeCr$_2$O$_4$)] or cohenite [(Fe,Ni,Co)$_3$C] (Norton, 2002) were hit, this will increase considerably the content of the elements Cr and Co. To avoid this nugget effect (Matheron, 1963), a larger statistical data set can be required to obtain reliable bulk concentrations using LMS. For optical inspection, to forecast a measurement on matrix material and to avoid measurements on inclusions, combination with a camera system will help with clarifications (Section 4).

In Table 3.2 the average values for the selected elements from all 138 measurements on the Allende sample are reported. Compared to the LMS results for Allende matrix alone (Table 3.1) it can be observed that the numbers differ slightly and since all measurements are included in the evaluation, the uncertainties

**Table 3.1**
Comparison of LMS results on Allende matrix with literature.

| Element | LMS measurement[b] | Clarke et al. (1971) |
|---|---|---|
| **Atomic fraction** | | |
| **Major elements**[a] | | |
| Mg | 0.1366 ± 0.0006 | 0.156 |
| Si | 0.13 ± 0.02 | 0.108 |
| Fe | 0.1072 ± 0.0004 | 0.143 |
| **Refractory siderophile**[a] | | |
| Co | (751 ± 15) ppm | 488 ppm |
| Ni | (7.51 ± 0.19) × 10$^{-3}$ | 11.9 × 10$^{-3}$ |
| **Refractory lithophile**[a] | | |
| Ca | (1.345 ± 0.014) × 10$^{-2}$ | 1.40 × 10$^{-2}$ |
| Al | (1.819 ± 0.005) × 10$^{-2}$ | 0.71 × 10$^{-2}$ |
| Ti | (530 ± 14) ppm | 318 ppm |
| V | (76 ± 7) ppm | – |
| Sc | (8 ± 1) ppm | – |
| **Moderate volatiles**[a] | | |
| Cr | (1.86 ± 0.02) × 10$^{-3}$ | 0.85 10$^{-3}$ |
| Mn | (734 ± 26) ppm | 909 ppm |
| S | (1.8 ± 0.1) × 10$^{-2}$ | 2.2 × 10$^{-2}$ |
| **Volatiles**[a] | | |
| C | (0.8 ± 0.7) × 10$^{-2}$ | 1.7 × 10$^{-2}$ |

[a] Cosmochemical classification from McSween and Huss (2010) according to condensation temperature of elements.
[b] Average on 66 LMS measurements that were optically found to be on Allende matrix.

**Table 3.2**
Comparison of LMS results on Allende bulk material.

| Element | LMS measurement[b] | Stracke et al. (2012) | Jarosewich (1990) |
|---|---|---|---|
| **Atomic fraction** | | | |
| ***Major elements***[a] | | | |
| Mg | $0.1263 \pm 0.0005$ | $0.1466 \pm 0.0072$ | $0.15 \pm 0.01$ |
| Si | $0.139 \pm 0.012$ | $0.137 \pm 0.002$ | $0.14 \pm 0.01$ |
| Fe | $0.1029 \pm 0.0003$ | $0.1014 \pm 0.0054$ | $0.10 \pm 0.01$ |
| ***Refractory siderophile***[a] | | | |
| Co | $(648 \pm 32)$ ppm | $(278 \pm 16)$ ppm | $(250 \pm 33)$ ppm |
| Ni | $(8.12 \pm 0.39) \times 10^{-3}$ | $(5.82 \pm 0.34) \times 10^{-3}$ | $(5.7 \pm 0.8) \times 10^{-3}$ |
| ***Refractory lithophile***[a] | | | |
| Ca | $(1.36 \pm 0.011) \times 10^{-2}$ | $(1.11 \pm 0.58) \times 10^{-2}$ | – |
| Al | $(1.821 \pm 0.004) \times 10^{-2}$ | $(1.524 \pm 0.785) \times 10^{-2}$ | $(1.5 \pm 0.1) \times 10^{-2}$ |
| Ti | $(686 \pm 56)$ ppm | $(451 \pm 170)$ ppm | $(450 \pm 59)$ ppm |
| V | $(86 \pm 6)$ ppm | $(46 \pm 0)$ ppm | – |
| Sc | $(12 \pm 2)$ ppm | – | – |
| ***Moderate volatiles***[a] | | | |
| Cr | $(1.83 \pm 0.01) \times 10^{-3}$ | $(1.68 \pm 0.11) \times 10^{-3}$ | $(1.6 \pm 0.014) \times 10^{-3}$ |
| Mn | $(578 \pm 15)$ ppm | $(643 \pm 45)$ ppm | $(610 \pm 70)$ ppm |
| S | $(2.02 \pm 0.29) \times 10^{-2}$ | – | $(1.5 \pm 0.033) \times 10^{-2}$ |
| ***Volatiles***[a] | | | |
| C | $(8.6 \pm 0.7) \times 10^{-3}$ | – | $(5.8 \pm 0.00) \times 10^{-3}$ |

[a] Cosmochemical classification from McSween and Huss (2010) according to condensation temperature of elements.
[b] Average on 138 LMS measurements on Allende bulk.

are generally smaller. While the concentrations of the mineral forming elements Mg, Si, Fe, Ca and Al stay basically unchanged, the content of the elements Ti, V, Ni or Sc e.g. is elevated. These refractory elements are preferentially contained in refractory chondrules of chondrites (Krot et al., 2007). The bulk analyses include measurements on chondrules, CAIs and other inclusions and thus higher concentrations of these elements can be expected.

For comparison, Table 3.2 displays also element concentrations for the Allende bulk analyses from (Stracke et al., 2012; Jarosewich, 1990). The bulk analyses in Stracke et al. (2012) are based on X-ray fluorescence (XRF) and inductively coupled plasma mass spectrometry (ICP MS) analyses of 39 pieces of Allende, about 0.6 g each, including a dark inclusion (DI) and a CAI. The data in Jarosewich (1990) were obtained by XRF on Allende bulk samples. Both reference data sets were converted from weight to atomic percent for comparison with LMS data.

The LMS measured content of Mn is lower in the bulk (Table 3.2) than in the matrix analyses (Table 3.1). This could be an indication that Mn-richer locations were included in the matrix measurements. The average concentration of Co is measured to be lower in the bulk than in the matrix, which implies that few grains of Co-bearing minerals included in the matrix analyses influence the results and Co concentrations are smoothed by higher statistics in the average of all 138 measurements. Taking into account the sample amount that was ablated by LMS for the average determination of Allende bulk element concentrations, the minor divergences for some elements can be understood by the nugget effect (Matheron, 1963). Whereas LMS uses only nanogram amounts of material for a complete concentration determination in 138 locations, the other methods consumed one to several grams of material for the bulk analyses.

The bulk spot-analyses can be used to constrain the mineralogy of the target material. In Fig. 3.1 the Ca-concentrations of the LMS measurements on Allende are plotted versus the Al concentrations, each relative to the sum of Mg and Fe. Additionally to the LMS Allende measurements, several mineralogical regions, including spinel, feldspars, clinopyroxene, olivine and orthopyroxene, are indicated. The Ca/Al ratio of anorthite, e.g. is defined by a 1:2 ratio, which in Fig. 3.1 is indicated by an arrow with the according slope pointing outwards as anorthite contains more Al than the
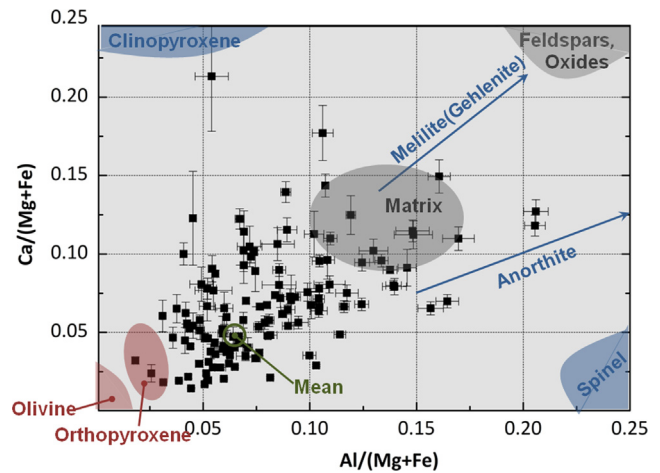


**Fig. 3.1.** Mineralogical analysis. By the ratios of Ca, Al, Mg and Fe, basic mineralogical classes are defined. It can be seen that the 138 LMS measurements on the Allende sample are mixtures of known minerals. The mean value is taken from McSween and Huss (2010) for CV chondrites in general and from Stracke et al. (2012) for Allende specifically.

scale in the figure. Additionally, a literature mean of the element ratios is shown, which includes the mean values for Allende and CV CC from other publications. By figures, these are

$$Al/(Mg+Fe)//Ca/(Mg+Fe)$$
$$= 0.061 \pm 0.031 // 0.045 \pm 0.023 \text{ (all Allende measurements from (Stracke et al., 2012))}$$
$$= 0.057 \pm 0.010 // 0.041 \pm 0.004 \text{ (Allende without CAI and DI from (Stracke et al., 2012))}$$
$$= 0.0624 // 0.046 \text{ (CC CV from (McSween and Huss, 2010))}.$$

The measured data of LMS on the Allende sample are distributed around these average values and all data points can be defined by mixtures of known minerals. Since olivine e.g. contains only very little Al and Ca, it shows that the LMS measurements did not hit a pure olivine grain. The same was found for spinel and clinopyroxene.

Many pure minerals within inclusions and chondrules in the Allende meteorite are known to be of cm size (e.g. large CAIs or spinel grains), but CAIs, spinel, olivine or nickel–iron grains occur in this inhomogeneous meteorite also in grain sizes of less than 1 μm (Grossman, 1975). As the laser beam of the current LMS setup is of ∼20 μm diameter (Section 3.1), it becomes evident that one measurement represents a mixture of different minerals. Fig. 2.3c shows the size of single grains in the chondrules of Allende. In most cases a randomly placed beam with a diameter of ∼20 μm will hit a mixture of different minerals. In the future, LMS will be equipped with an integrated camera system, with which it will be possible to target individual grains (Section 4).

### 3.3. Mineralogical maps

Fig. 3.2 shows the concentrations of Ca for all measured locations. The markers are oversized for better legibility. The Ca-abundance is shown in units of atomic fraction, referring to the abundance of Ca-atoms in one measurement.

It can be seen that the matrix measurements (black markings in Fig. 2.3b) contain about 1.5 at% Ca (Table 3.1). Measurements on chondrules or inclusions show a much larger spread in their Ca-concentrations. In general, lighter coloured areas of the meteorite sample have higher Ca-concentrations (see colour bar in Fig. 3.2). Some of these locations could represent CAIs. A very light-grey inclusion at $(x/y) \approx (+0.2 \text{ mm} / +5.8 \text{ mm})$ was found to contain very little Ca. Darker coloured areas contain less Ca and can be
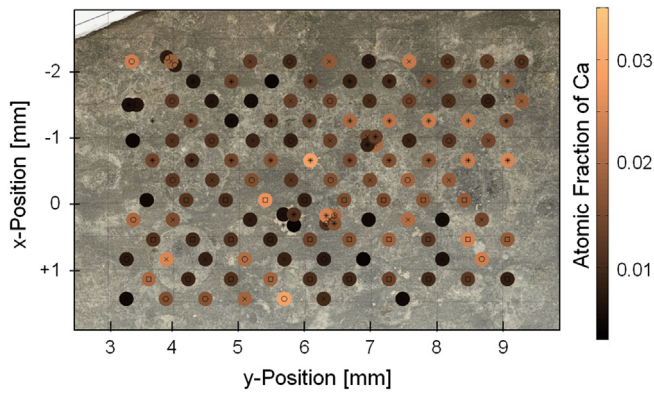
**Fig. 3.2.** Map of calcium on Allende surface. The map shows the abundance of Ca for the investigated locations. Sampled spots are of 20 μm diameter, but are displayed larger for clarity. Background image is the same as Fig. 2.3b. The *x*-position is drawn on the *y*-axis and the *y*-position on the *x*-axis according to the denotation of the micro-translational stage (coordinate system in Fig. 2.1).

found in regions that also differ optically from the relatively homogeneous light-grey matrix material. From Tables 3.1 and 3.2 it can be seen that the average Ca-content of the Allende bulk analysis does not differ significantly from that of matrix measurements. This leads to the conclusion that no large CAI was sampled in this measurement series on the Allende meteorite, which can also be concluded from Fig. 3.1 in Section 3.2.

Maps similar to the one in Fig. 3.2 are available for all evaluated elements. Plotting element ratio maps instead can be used to identify the modal mineralogy of the sample material. This makes LMS unique as kind of in situ element imaging instrument.

### 3.4. Allende CV3 depletion in volatile elements

It is a well known fact that due to their formation processes, the terrestrial planets as well as chondritic meteorites of class CV3 are depleted in volatile elements (Bland et al., 2005). This depletion is also seen in the Allende data measured by LMS.

In Fig. 3.3a the content of various elements relative to the elemental content of CI chondrites (from (Lodders, 2003)) is shown. The elements on the *x*-axis are sorted by their 50% condensation temperature at a total pressure of $10^{-4}$ bar (from (Lodders, 2003)) starting from very volatile elements on the right side to refractory elements on the left side of the diagram. Fig. 3.3a shows the curves of five example LMS measurements on the Allende matrix. The exact position of the measurement locations on the meteorite sample is shown in Fig. 2.3d, where the points are marked with M1 to M5 in black, according to the labels in Fig. 3.3a. The plot demonstrate that these five points on Allende matrix material show a similar dependence on the condensation temperature. The matrix material is clearly depleted in volatile elements. Also the finding that CV chondrites are more enriched in lithophile (Ca, Al, and Ti) than siderophile (Co, Ni) elements compared to CI chondrites (Scott and Krot, 2005) is confirmed by these measurements.

Fig. 3.3b displays six LMS measurements on the Allende surface that are not located on matrix material. The six points are marked in Fig. 2.3d as P1 to P6 in red. As expected, the elemental content on chondrules, inclusions and similar specific regions on the meteorite surface varies much more than in the matrix material. Point P2 represents an anomalous composition with low abundance of refractory elements and a large excess of S and a relative depletion in Fe. This point can be correlated with a very light-coloured inclusion on the sample surface (see Fig. 2.3d). Comparing with Fig. 3.2 it is the same inclusion at $(x/y) \approx (+0.2\ mm/+5.8\ mm)$ that showed a very
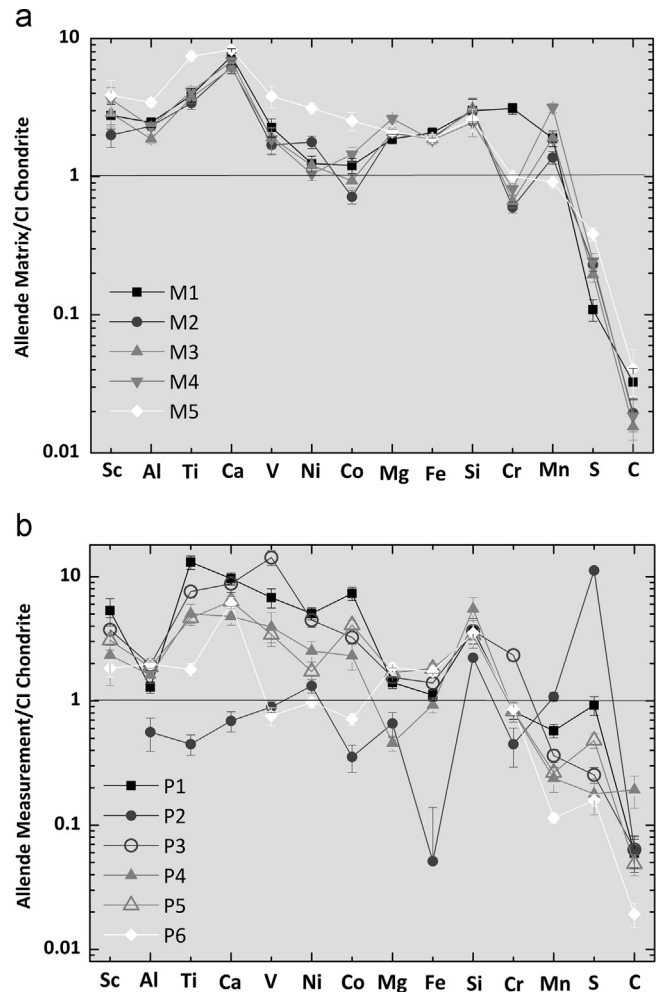


**Fig. 3.3.** Element abundances in Allende relative to CI chondrite. (a) The elemental content of five example LMS measurements on the Allende matrix (M1 to M5 identified in Fig. 2.3d) relative to CI abundance (Lodders, 2003) is shown over the 50% condensation temperature (Lodders, 2003) of the elements. (b) The elemental content of six LMS measurements on non-matrix locations on Allende (P1 to P6 identified in Fig. 2.3d) relative to CI chondrite is displayed over the 50% condensation temperature (at $10^{-4}$ bar) (Lodders, 2003) of the elements.

low concentration of Ca. These findings could indicate that this inclusion contains a sulphide phase, possibly CaS (oldhamite).

Fig. 3.4 shows the average value of the matrix (Table 3.1) and of all 138 LMS measurements (Table 3.2) on the Allende sample relative to CI chondrite over the 50% condensation temperature (from (Lodders, 2003)). For comparison, the values from (Stracke et al., 2012) are also plotted. They comprise the bulk concentration and for selected measurements neglecting a large calcium–aluminium-rich inclusion (CAI) and a dark inclusion (DI). The data are in very good agreement and reveal the high depletion in volatiles of the Allende meteorite. This depletion in volatile elements reflects the history of the carbonaceous chondrite Allende from its formation out of the early solar nebula until condensation and chondrule formation (Kleine et al., 2005).

## 4. Conclusion and outlook

On the surface of an Allende sample 138 measurements of the elemental content have been carried out with the miniature laser ablation mass spectrometer LMS. The elemental abundances of the elements C, Mg, Al, Si, S, Ca, Sc, Ti, V, Cr, Mn, Fe, Co and Ni were measured and evaluated. The obtained concentration of these
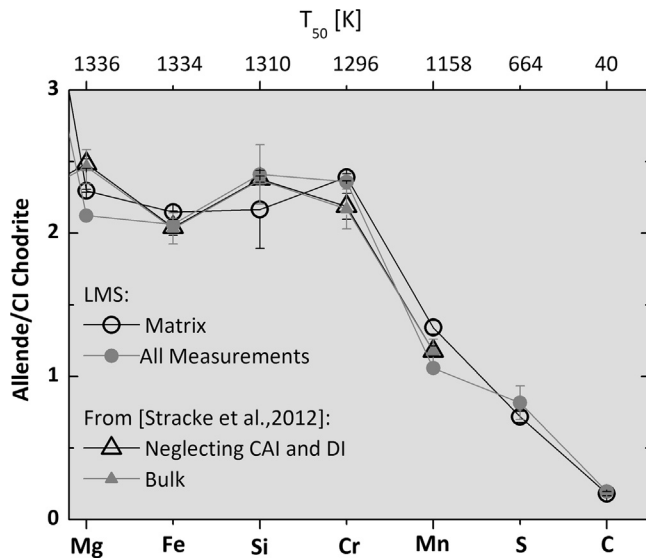
**Fig. 3.4.** Allende/CI chondrite for moderately volatile elements. This plot shows the LMS measurements on the Allende matrix (Table 3.1) and the mean of all 138 measurements (Table 3.2) in relation to CI chondrite (from (Lodders, 2003)) over the 50% condensation temperature at $10^{-4}$ bar (from (Lodders, 2003)). For comparison, the data from (Stracke et al., 2012)) are displayed. The results agree very well with the reference data and emphasize the depletion in volatile elements in the carbonaceous chondrite Allende.

elements in Allende matrix and bulk agree well with published data of Allende (Stracke et al., 2012; Jarosewich, 1990; Clarke et al., 1971). This underlines that LMS is a well suited instrument to measure elemental abundances on a planetological surface or alike.

One measurement of this campaign, i.e. 50,000 laser single spectra, took ~40 min to be recorded with 20 Hz repetition rate of the laboratory laser system. Nevertheless, for the in situ application a passively Q-switched laser source with a repetition rate 1–10 kHz laser is planned to be applied, which will make it possible to record the same data in 5 s. Additionally, the surface ablation and ionisation processes using such a fast laser, are

The mass calibration of the TOF spectra in this study was performed individually for every measurement and channel. Analysis of the mass scale calibration characteristics showed that the calibration parameters remain constant and are independent of applied laser irradiance (Section 2.3). This indicates robustness of the experimental configuration of LMS in a long measurement campaign (~100 h for all 138 measurements) and demonstrates the good reproducibility of measurements. For an LMS operating in space, long term robustness and therefore failure-safe operation is an important requirement. An upgrade of the LMS software is planned, where a robust automatic spectrum calibration will be implemented using the calibration constants quantified in this study as starting values in case they are needed by the auto-calibration algorithm.

Our Allende measurements with LMS also confirmed that the use of three channels with different gain factors for signal acquisition allows the effective detection of major to trace elements. By combining the data from three channels in the data evaluation a high dynamic range is reached and major elements were analysed as well as minor and trace elements. Trace elements down to the ppm level, like Sc and V can be measured quantitatively. This makes LMS a unique instrument for in situ space research by detecting all elements in the range between 1 and 250 amu in solid materials in one measurement with high accuracy and mass resolution.

The results of the chemical composition of the matrix measurements indicate a very consistent agreement with literature data, which strongly demonstrates the applicability of the LMS measurements for such investigations. The quantitative elemental bulk analysis of the Allende surface was found to agree with established

data, with the exception of minor differences to literature values for few elements, e.g. Co. These differences can be explained by the small sample consumption and small size of the sampled locations investigated by LMS. Compared to other methods for elemental composition determination, the sample consumption in LMS is minimal. In this study, 50,000 laser shots were applied in one measurement, which equals a sample consumption of approximately 30 pg in one measurement location and about 3 ng for the entire measurement campaign (Section 3.1). In future studies it is planned to apply less laser shots, which will reduce the sample consumption further. It has to be emphasized that in principle already one laser shot provides the complete chemical composition of the sample. However, the averaging is needed to increase the dynamic range of the measurement and a reliable bulk analysis requires a large data set of individual measurements.

Concentration measurements for Allende matrix as well as measurements on chondrules and inclusions were correlated with an optical image of the sample surface. On the basis of an elemental map for Ca it could be demonstrated that such maps can be established for all measured elements. This makes LMS an elemental imaging instrument having a spatial resolution in the ~10 μm range. The property of laser ablation also makes it possible to analyse a depth profile of the sample (Tulej et al., 2012). Considering the very small ablation rate (0.1 μm by 50,000 laser shots) means a high spatial vertical resolution. The high horizontal spatial resolution combined with the high detection sensitivity allowed resolving the large compositional inhomogeneity of the Allende meteorite. If no or very limited sample preparation is possible, like on a space mission, it is therefore a key issue to measure the chemical composition with high spatial resolution, to separate for example the chondrule compositions from the matrix on a grain size scale.

In a mineralogical analysis of the Allende data, it was confirmed that the measurements contain mixtures of different mineral phases. By identifying element ratios of defined minerals in single in situ measurements, LMS measurements allow to reveal the mineralogical composition of a rock as it would be of large interest on a planetary or alike surface. The LMS analyses confirmed the volatile element depletion of the Allende sample and the elemental abundances measured are both in good agreement with literature data.

The performance of LMS as an instrument for application in space servicing the purposes of measuring elemental abundances and thus derive the mineralogical compositions of rocks was demonstrated. The high spatial resolution and the ability to measure major and trace elements at once in a fast and essentially non-destructive way make LMS a powerful instrument with a wide range for different analyses to study the isotopic, elemental and mineralogical composition of natural heterogeneous solids on a planetary surface.

### Acknowledgement

### Appendix A

In previous studies NIST standard materials and a sample of homogenized Allende (powdered and pressed to a pellet) were investigated. In each study, the laser irradiance and also the other parameters like the voltages for the reflectron and the MCPs were
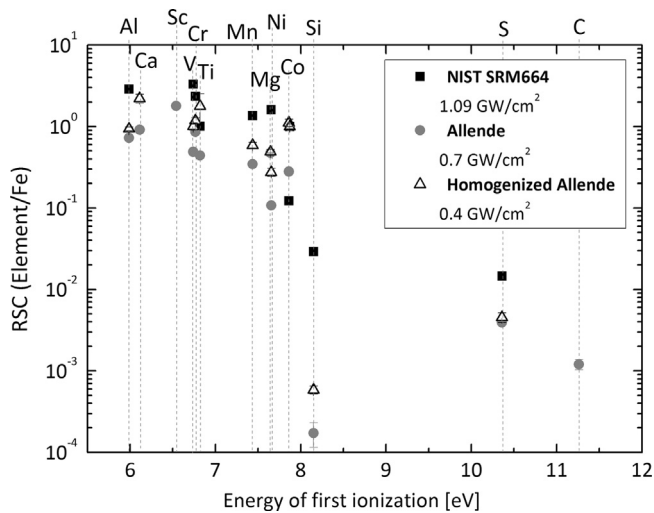
**Fig. A.1.** Correlation of RSCs on energy of first ionisation. RSCs for Al, Ca, Sc, V, Cr, Ti, Mn, Mg, Ni, Co, Fe, Si, S and C over their energy of first ionization. In the study of NIST SRM664 it was not possible to determine the RSCs of Al, Ca and Sc.

optimized for best performance regarding mass resolution, signal intensity and sensitivity. As the NIST SRM664 is a carbon-steel sample, it generally differs from the Allende samples in its composition. Additionally this metal sample has a much more compact texture, which leads to the need of a higher laser irradiance for the measurements. On the contrary, the pellet of homogenized Allende has an even higher porosity than the Allende meteorite sample used in this study, which made a lower laser irradiance more suitable for the measurements.

Fig. A.1 displays the RSCs (relative to Fe) from the three different campaigns over the ionisation energy of the according element (second column in Table 2.3). The numbers for Allende (0.7 GW/cm$^2$) are the RSCs gained from this study. For all three samples, the RSCs show the general correlation to be smaller with increasing ionisation energy, which is expected from the process of plasma generation and ionisation by the laser-surface interaction. On NIST SRM664, due to the morphology of the sample, a higher irradiance had to be applied for optimal LMS performance, which results in higher RSC values also for the elements with higher ionisation potential, like Si for example. At the same time, NIST SRM664 does not contain Ca and Sc. Therefore no RSC was determined for these elements.

The overall uniformity of the RSCs calculated in this study and previously gained RSC values on other samples, confirms the reliability of the RSCs for Allende. RSCs over potential of first ionisation in laser ablation application with a ns-laser were also reported by other groups. In Zhang et al. (2013) the authors present a similar trend of RSCs. At the same time, the differences between the RSCs from all three studies for each element (Fig. A.1) state that it is necessary to determine the RSC sets on a reference sample that has preferably similar texture and composition to the sample of study.

# References

Amoruso, S., Bruzzese, R., Spinelli, N., Velotta, R., 1999. Characterization of laser-ablation plasmas. J. Phys. B: At. Mol. Opt. Phys. 32 (14), R131–R172.
Astronomy & Geophysics, 2012. Phobos-Grunt's Sad Return 53, 1.10–1.11.
Balogh, A., Bird, M., Blomberg, L., Bochsler, P., Bougeret, J.-L., Brückner, J., Iess, L., Guest, J., Langevin, Y., Milani, A., Sauvaud, J.-A., Schmidt, W., Spohn, T., von Steiger, R., Thomas, N., Torkar, K., Wänke, H., Wurz, P., 2000. BepiColombo—An Interdisciplinary Cornerstone Mission to the Planet Mercury, ESA-SCI (2000)1. European Space Agency, Noordwijk, The Netherlands
Barucci, M.A., Dotto, E., Levasseur-Regourd, A.C., 2011. Space missions to small bodies: asteroids and cometary nuclei, 2011. Astron. Astrophys. Rev. 19 (48), 29.
Barucci, M.A., Cheng, A.F., Michel, P., Benner, L.A.M., Binzel, P.A., Böhnhardt, H., Brucato, J.R., Campo Bagatin, A., Cerroni, P., Dotto, E., Fitzsimmons, A., Frachni, I. A., Green, S.F., Lara, L.-M., Licandro, J., Marty, B., Muinonen, K., Nathues, A., Oberst, J., Rivkin, A.S., Robert, F., Saladino, R., Trigo-Rodriguez, J.M., Ulamec, S., Zolensky, M., 2012. MarcoPolo-R near earth asteroid sample return mission. Exp. Astron. 33 (2-3), 645–684.
Bazalgette Courrèges-Lacoste, G., Ahlers, B., Pérez, F.R., 2007. Combined Raman spectrometer/laser-induced breakdown spectrometer for the next ESA mission to Mars. Spectrochim. Acta, Part A 68 (4), 1023–1028.
Becker, J.S., 2007. Inorganic Mass Spectrometry: Principles and Applications, first ed. John Wiley & Sons p. 514
Bieler, A., Altwegg, K., Hofer, L., Jäckel, A., Riedo, A., Sémon, T., Wahlström, P., Wurz, P., 2011. Optimization of mass spectrometers using the adaptive particle swarm algorithm. J. Mass Spectrom. 46 (11), 1143–1151.
Bland, P.A., Alard, O., Benedix, G.K., Kearsley, A.T., Menzies, O.N., Watt, L.E., Rogers, N.W., 2005. Volatile fractionation in the early solar system and chondrule/matrix complementarity. Proc. Nat. Acad. Sci. U.S.A. 102 (39), 13755–13760.
Bonal, L., Quirico, E., Bouro-Denise, M., Montagnac, G., 2006. Determination of the petrologic type of CV3 chondrites by Raman spectroscopy of included organic matter. Geochim. Cosmochim. Acta 70 (7), 1849–1863.
Brinckerhoff, W.B., Managadze, G.G., McEntire, R.W., Cheng, A.F., Green, W., 2000. Laser time-of-flight mass spectrometry for space. Rev. Sci. Instrum 71 (2), 536–545.
Brucato, J.R., Rotundi, A., Mazotta Epifani, E., 2009. Sample return missions from minor bodies: achievements, future plan and observational support. Earth Moon Planets 105, 273–282.
Bulgakova, N.M., Bulgakov, A.V., Bobrenok, O.F., 2000. Double laser effects in laser-ablation plasma plumes. Phys. Rev. E: Stat. Nonlinear Soft Matter Phys. 62 (4), 5624–5635.
Clarke Jr., R.S., Jarosewich, E., Mason, B., Nelen, J., Gomez, M., Hyde, J.R., 1971. The Allende Mexico, Meteorite Shower. Smith Cont. Earth Sci. 5, 1–53.
Consolmagno, G.J., Britt, D.T., 1998. The density and porosity of meteorites from the Vatican collection. Meteorit. Planet. Sci 33 (6), 1231–1241.
Figg, D.J., Cross, J.B., Brink, C., 1998. More investigations into elemental fractionation resulting from laser ablation-inductively coupled plasma-mass spectrometry on glass samples. Appl. Surf. Sci. 127-129, 287–291.
Grossman, L., 1975. Petrography and mineral chemistry of Ca-rich inclusions in the Allende meteorite. Geochim. Cosmochim. Acta 39 (4), 433–434 (IN1–IN2, 435–454).
Harilal,S.S., Bindhu, C.V., Najmabadi, F., Gaeris, A.C., Internal structure and expansion dynamics of laser ablation plumes into ambient gases, J. Appl. Phys. 93(5), 2380–2388.
Huang, R., Yu, Q., Li, L., Lin, Y., Hang, W., He, J., Huang, B., 2011. High irradiance laser ionization orthogonal time-of-flight mass spectrometry: a versatile tool for solid analysis. Mass Spectrom. Rev. 30 (6), 1256–1268.
Jarosewich, E., 1990. Chemical analyses of meteorites: a compilation of stony and iron meteorite analyses. Meteoritics 25, 323–327.
Khartov, V.V., Zelenyi, L.M., Dolgopolov, V.P., Efanov, V.V., Zaytseva, O.N., Lukiyan-chikov, A.V., Martynov, M.B., Pichkhadze, K.M., New Russian lunar unmanned space complexes, Sol. Syst. Res. 45(7):690-696.
Kim, S.S, Hayati, S., Lavery, D., McBride, K.S., 2006. Mars Miniature Science Instruments. IEEE Aerospace Conference, New Jersey, pp. 1–11
Kleine, T., Mezger, K., Palme, H., Scherer, E., Münker, C., 2005. Early core formation in asteroids and late accretion of chondrite parent bodies: evidence from $^{182}$Hf–$^{182}$W in CAIs, metal-rich chondrites, and iron meteorites. Geochim. Cosmochim. Acta 69 (24), 5805–5818.
Krot, A.N., Keil, K., Scott, E.R.D., Goodrich, C.A., Weisberg, M.K., 2007. 1.05—classification of meteorites. Treatise Geochem. 1, 1–52.
Lawrence, D.J., Feldman, W.C., Barraclough, B.L., Binder, A.B., Elphic, R.C., Maurice, S., Thomsen, D.R., 1998. Global element maps of the moon: the Lunar Prospector gamma-ray spectrometer. Science 281 (5382), 1484–1489.
Lin, Y., Yu, Q., Hang, W., Huang, B., 2010. Progress of laser ionization mass spectrometry for elemental analysis—a review of the past decade. Spectrochim. Acta, Part B 65 (11), 871–883.
Lodders, K., Fegley Jr., B., 1998. The Planetary Scientist's Companion. Oxford University Press, New York p. 392
Lodders, K., 2003. Solar system abundances and condensation temperatures of the elements. Astrophys. J. 591 (2), 1220–1247.
MacPherson, G.J., Thiemens, M.H., 2011. Cosmochemistry: understanding the solar system through analysis of extraterrestrial materials. Proc. Nat. Acad. Sci. U.S.A 108 (48), 19130–19134.
Managadze, G.G., Wurz, P., Sagdeev, R.Z., Chumikov, A.E., Tulej, M., Iakovleva, M., Managadze, N.G., Bondarenko, A.L., 2010. Study of the main geochemical characteristics of Phobos' regolith using laser time-of-flight mass spectrometry. Sol. Syst. Res 44 (5), 376–384.
Matheron, G., 1963. Principles of geostatistics. Econ. Geol. 58 (8), 1246–1266.
McSween Jr., H.Y., Huss, G.R., 2010. Cosmochemistry. Cambridge University Press
McSween Jr., H.Y., McNutt Jr., R.L., Prettyman, T.H., 2011. Spacecraft instrument technology and cosmochemistry. Proc. Nat. Acad. Sci. U.S.A 108 (48), 19177–19182.
Meyer, S., 2013. Development of a Fully Automated and Highly Precise Data Analysis for a Miniaturized Laser-Ablation Mass Spectrometer, Masterthesis, Space Research and Planetary Sciences. University of Bern
Moskalenko, I.V., Porter, T.A., 2007. The gamma-ray Albedo of the moon. Astrophys. J. 670, 1467–1472.

Norton, O.R., 2002. The Cambridge Encyclopedia of Meteorites. Cambridge University Press

Rieder, R., Gellert, R., Brückner, J., Klingelhöfer, G., Dreibus, G., Yen, A., Squyres, S.W., 2003. The new Athena alpha particle X-ray spectrometer for the mars exploration rovers. J. Geophys. Res. 108 (E12), 13 (8066).

Riedo, A., Bieler, A., Neuland, M., Tulej, M., Wurz, P., 2012. Performance evaluation of a miniature laser ablation time-of-flight mass spectrometer designed for in-situ investigations in planetary space research. J. Mass Spectrom. 48, 1–15 (2013).

Riedo, A., Meyer, S., Heredia, B., Neuland, M.B., Bieler, A., Tulej, M., Iakovleva, M., Mezger, K., Wurz, P., 2013a. Highly accurate isotope composition measurements by a miniature laser ablation mass spectrometer designed for in situ investigations on planetary surfaces. Planet. Space Sci. 87, 1–13.

Riedo, A., Neuland, M., Meyer, S., Tulej, M., Wurz, P., 2013b. Coupling of LMS with a fs-laser ablation ion source: elemental and isotope composition measurements. J. Anal. At. Spectrom., 2013 28 (8), 1256–1269.

Rohner, U., Whitby, J., Wurz, P., 2003. A miniature laser ablation time-of-flight mass spectrometer for in situ planetary exploration. Meas. Sci. Technol. 14, 2159–2164.

Rohner, U., Whitby, J.A., Wurz, P., Barabash, S., 2004. Highly miniaturized laser ablation time -of-flight mass spectrometer for a planetary rover. AIP, Rev. Sci. Instrum., 75; , pp. 1314–1322.

Russo, R.E., Mao, X., Liu, H., Gonzalez, J., Mao, S.S., 2002. Laser ablation in analytical chemistry—a review. Talanta 57 (3), 425–451.

Scott, E.R.D., Krot, A.N., 2005, Chondritic meteorites and the high-temperature nebular origins of their components, chondrites and the protoplanetary disk, In: ASP Conference of Proceedings. 341, 15-53.

Stracke, A., Palme, H., Gellissen, M., Münker, C., Kleine, T., Birbaum, K., Günther, D., Bourdon, B., Zipfel, J., 2012. Refractory element fractionation in the Allende meteorite: Implications for solar nebula condensation and the chondritic composition of planetary bodies. Geochim. Cosmochim. Acta 85, 114–141.

Taylor, G.J., Boynton, W., Brückner, J., Wänke, H., Dreibus, G., Kerry, K., Keller, J., Reedy, R., Evans, L., Starr, R., Squyres, S., Karunatillake, S., Gasnault, O., Maurice, S., d'Uston, C., Englert, P., Dohm, J., Baker, V., Hamara, D., Janes, D., Sprague, A., Kim, K., Drake, D., 2006. Bulk composition and early differentiation of Mars. J. Geophys. Res. 111 (E03S10), 148–227.

Tulej, M., Iakovleva, M., Leya, I., Wurz, P., 2011. A miniature mass analyser for in situ elemental analysis of planetary material: performance studies. Anal. Bioanal. Chem. 399, 2185–2200.

Tulej, M., Riedo, A., Iakovleva, M., Wurz, P., 2012. On applicability of a miniaturized laser ablation time of flight mass spectrometer for trace element measurements. Int. J. Spectrom., 14 (article ID 234949)

Tulej, M., Riedo, A., Neuland, M.B., Iakovleva, M., Wurz, P. Element alanalysis of planetary surface: overview of concepts, instrumentation and results, 2013. Appl. Spectrosc. Rev, in preparation.

Tulej, M., Riedo, A., Neuland, M., Meyer, S., Thomas, N., Wurz, P. Aminiature instrument suite for investigation of composition and morphology of asteroidal materials (CAMAM). Geoscientific Instrum. Methods Data Syst. (GID) (submitted for publication).

Wurz, P., Whitby, J., Managadze, G., 2009, Laser Mass Spectrometry in Planetary Science, AIP Conference of Proceedings. CP1144, 70-75.

Wurz, P., Abplanalp, D., Tulej, M., Iakovleva, M., Fernandes, V.A., Chumikov, A., Managadze, G.G., 2012. Mass spectrometric analysis in planetary science: investigation of the surface a and the atmosphere. Sol. Syst. Res 46 (6), 408–422.

Xie, X., Huang, F., Wie, X., Hu, W., Ren, Q., Yuan, X., 2011. Ablation threshold of sapphire by pulsed green laser in nanosecond regime. Adv. Manuf. Technol. 1-3 (314-316), 1930–1934 (in Advanced Materials Research).

Yu, Q., Cao, Z., Li, L., Yan, B., Hang, W., He, J., Huang, B., 2009. Femtogram detection and quantitation of residues using laser ionization orthogonal time-of-flight mass spectrometry. Anal. Chem. 81 (20), 8623–8626.

Zhang, B., He, M., Hang, W., Huang, B., 2013. Minimizing matrix effect by femtosecond laser ablation and ionization in elemental determination. Anal. Chem. 85, 4507–4511.

Zinner, E.K., Moynier, F., Stroud, R.M., 2011. Laboratory technology and cosmochemistry. Proc. Nat. Acad. Sci. U.S.A. 108 (48), 19135–19141.